2010

Theoretical Analysis of Stresses in a Lithium Ion Cell

Sindhuja Renganathan
University of South Carolina, renganat@email.sc.edu

Godfrey Sikha
University of South Carolina - Columbia

Shriram Santhanagopalan

Ralph E. White
University of South Carolina - Columbia, white@cec.sc.edu

Publication Info

Published in *Journal of the Electrochemical Society*, Volume 157, Issue 2, 2010, pages A155-A163.

Renganathan, S., Sikha, G., Santhanagopalan, S., & White, R.E. (2010). Theoretical Analysis of Stresses in a Lithium Ion Cell. *Journal of the Electrochemical Society*, *157*(2): A155-A163.
Publisher's Version: http://dx.doi.org/10.1149/1.3261809

Journal of The Electrochemical Society, **157** (2) A155-A163 (2010)
0013-4651/2009/157(2)/A155/9/$28.00 © The Electrochemical Society

Theoretical Analysis of Stresses in a Lithium Ion Cell

Sindhuja Renganathan,[a,*] Godfrey Sikha,[a,,c] Shriram Santhanagopalan,[b,**] and Ralph E. White[a,***,z]**

[a]*Department of Chemical Engineering, University of South Carolina, Columbia, South Carolina 29208, USA*
[b]*Celgard LLC, Charlotte, North Carolina 28273, USA*

A mathematical model to simulate the generation of mechanical stress during the discharge process in a dual porous insertion electrode cell sandwich comprised of lithium cobalt oxide and carbon is presented. The model attributes stress buildup within intercalation electrodes to two different aspects: changes in the lattice volume due to intercalation and phase transformation during the charge/discharge process. The model is used to predict the influence of cell design parameters such as thickness, porosity, and particle size of the electrodes on the magnitude of stress generation. The model developed in this study can be used to understand the mechanical degradation in a porous electrode during an intercalation/deintercalation process, and the use of this model results in an improved design for battery electrodes that are mechanically durable over an extended period of operation.
 [DOI: 10.1149/1.3261809]

Manuscript submitted August 24, 2009; revised manuscript received October 16, 2009. Published December 14, 2009. This was Paper 210 presented at the San Francisco, California Meeting of the Society, May 24–29, 2009.

Lithium ion based rechargeable batteries (LIBs) have become one of the most desirable power sources for many portable consumer applications. LIB has also been tapped as a potential candidate for high power applications such as electric and hybrid electric vehicles.[1] In recent years many improvements have been made to increase the performance and life of the battery. Many potential concerns such as thermal abuse,[2] lithium deposition,[3] porosity change, film formation, and other side reactions[4-6] have been identified, and studies have been conducted to understand the resultant capacity loss. Stress generation due to the intercalation process has been shown to produce cracks or fractures in the material[7,8] which can lead to failure of the battery. Out of the possible factors that reduce the performance and durability of the battery, mechanical stress arising in the battery electrodes is the least studied. Kostecki and McLarnon conducted a microprobe study on graphite electrode and found that an increase in the structural degradation of a graphite electrode caused an increase in the amount of side reaction products formed,[9] hence indicating a possible correlation between both these modes of failure. It is imperative to understand the various failure modes and their individual and mutual roles in reducing the life of the battery. To achieve this goal, a systematic approach is necessary to correlate the various processes that occur during the operation of the battery with its performance. One such approach is to simulate the behavior of the battery using a comprehensive mathematical model that includes the various failure modes.

Mathematical models that include the generation of stress during intercalation and de-intercalation processes have been used previously to study lithium manganese oxide[10,11] and carbon electrodes[12] by Christensen and Newman under galvanostatic conditions. Zhang et al.[13] included stress generation in single electrode particles under potentiodynamic conditions. Recently Cheng and Verbrugge[14] presented an analytical solution for stress generation in a spherical particle under galvanostatic and potentiostatic conditions. However, these models are developed for a single electrode particle and do not consider the porous nature of the electrode. Some of these studies[11-14] have not considered the stress arising due to the phase transformation in their models.

To the authors' knowledge, the only theoretical work that considered stress generation in the porous intercalation electrode was presented by Garcia et al.,[15] which considered a two-dimensional (2D) model geometry with spherical particles distributed within the electrode, to predict the performance of the battery and stress distribution. The importance of this work is that the framework used in the study can be employed to simulate the performance of battery electrodes with complex microstructures, i.e., electrodes with severe particle aggregations and multiple particle sizes and shapes. This approach is better suited for qualitative understanding of the structure-mechanical stability-performance relationships in a battery electrode. But extension of this model as a predictive tool to quantitatively estimate life and capacity of the battery during charge/discharge cycles becomes computationally intensive because the model equations need to be solved simultaneously in two spatial directions, and there is an additional cost involved in creating a digital facsimile of the electrode microstructure.

In the present work we take advantage of the porous electrode theory along with the pseudo-2D approach[16,17] to model the battery electrodes, which enables us to maintain the necessary rigor required for making accurate predictions and at the same time reduce the computational cost considerably. This work also includes the nonlinearity associated with the electrolyte phase and the phase transformations taking place in the solid phase which have not been considered in Ref. 15. The objective of our study is to use a comprehensive mathematical model to (*i*) develop a correlation between the mechanical properties and performance of the porous battery electrodes and (*ii*) understand the importance of the structural and mechanical properties of the electrodes in determining the durability of the battery electrodes for a given set of operating conditions. To accomplish these goals, a pseudo-2D model is developed which takes into account (*i*) diffusion into the intercalation electrode particles (solid phase), (*ii*) stress generation due to intercalation and phase transformation processes in the electrode particles, (*iii*) diffusion and migration in the electrolyte (solution phase), and (*iv*) electrochemical reaction at the solid/solution interface.

Model Development

The schematic of the lithium ion battery system considered in this study is shown in Fig. 1. The battery consists of two porous intercalation electrodes: a positive electrode (Li_xCoO_2) and a negative electrode (carbon) with a porous separator between them and a liquid electrolyte throughout. The particles that make up the intercalation electrodes are assumed to be spherical. During the discharge process the lithium ion (de)intercalates from the negative electrode particles, diffuses and migrates through the electrolyte, and intercalates into the positive electrode particles. These processes are described with the help of a porous electrode model.[18] Many authors have successfully used the porous electrode theory in the past to model the lithium ion battery,[3-6,16-19] wherein detailed dis-

* Electrochemical Society Student Member.
** Electrochemical Society Active Member.
*** Electrochemical Society Fellow.
[c] Present address: Applied Materials Incorporation, Santa Clara, CA 95054, USA.
[z] E-mail: white@cec.sc.edu

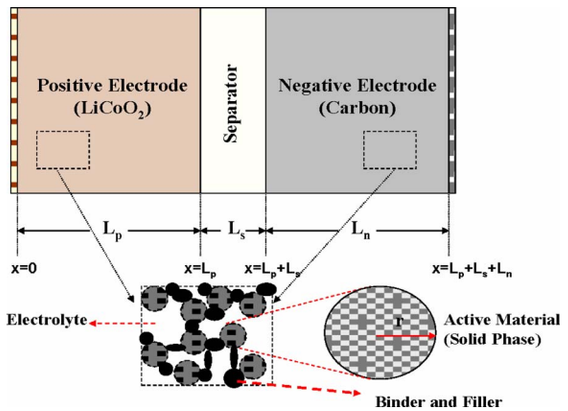

Figure 1. (Color online) Schematic of a lithium ion cell sandwich consisting of porous positive and negative electrodes and a porous separator.

cussions of the model and the governing equations are available. Hence only a summary of the equations is presented here.

The set of governing equations for the model system can be conveniently divided into four sections. In the first section the governing equations for mass transport in the solution phase, charge transport of lithium in the solid and solution phases of the porous electrode, and the kinetic expressions are summarized. In the second section the governing equations for the diffusion process inside the intercalation electrode particles are described. In the subsequent section the diffusion equations are modified to account for the phase transformation taking place in the electrode. In the final section, the governing equations describing the generation of mechanical stress in the intercalation particles are presented.

Porous electrode model.— The model equations to describe the solid and solution phase potentials, respectively, are

$$\nabla(\sigma^{\text{eff}} \nabla \phi_1) - J = 0 \qquad [1]$$

$$\nabla(\kappa^{\text{eff}} \nabla \phi_2) + \nabla(\kappa_D \nabla \ln C_2) + J = 0 \qquad [2]$$

where σ^{eff} and κ^{eff} are solid and solution phase effective conductivities, respectively, and κ_D is the diffusional conductivity. The solution phase concentration is described by the following equation

$$\frac{\partial(\varepsilon_2 C_2)}{\partial t} = \nabla(D_2^{\text{eff}} \nabla C_2) + \frac{1 - t^+}{F} J \qquad [3]$$

where D_2^{eff} is the effective diffusion coefficient in the solution phase of the porous electrode. The effective properties used in the above equations are discussed in detail elsewhere.[19] A list of expressions used in this study is presented in the Appendix.

The electrochemical reaction at the surface of the electrode particles is described using a Butler–Volmer type kinetic expression which is written as

$$J_i = a_i i_{0,i}\left[\exp\left(\frac{\alpha_a F}{RT}\eta_i\right) - \exp\left(-\frac{\alpha_c F}{RT}\eta_i\right)\right] \quad i = p, n \qquad [4]$$

where $i_{0,i}$ is the exchange current density for region i and is given by the following expression

$$i_{0,i} = k_i (C_2)^{\alpha_a} (C_{1,i}^s)^{\alpha_c} (C_{1,i}^{\max} - C_{1,i}^s)^{\alpha_a} \quad i = p, n \qquad [5]$$

The overpotential for the electrochemical reaction is expressed as

$$\eta_i = \phi_1 - \phi_2 - U_i^{\text{ref}} \quad i = p, n \qquad [6]$$

where U_i^{ref} is the open-circuit potential of the intercalation electrode in region i, which is a function of the state of charge (SOC) or concentration at the particle surface.

Diffusion inside the solid phase.— The intercalation material is assumed to be a binary solution as treated by Christensen and Newman,[12] then the flux of lithium (with composition gradient and pressure as driving forces) within the particle can be described by using the generalized Maxwell–Stefan equation[20]

$$N_{1,i} = -D_{1,i}\left[\frac{\partial}{\partial r}(C_{1,i}) + \frac{C_{1,i}}{RT}\left(\bar{V}_{1,i} - \frac{M_i}{\rho_i}\right)\frac{\partial}{\partial r}(P_i)\right] \quad i = p, n \qquad [7]$$

The thermodynamic pressure term (P) in Eq. 7 can be replaced by the hydrostatic stress (σ_h). The resulting equation is given by[21]

$$N_{1,i} = -D_{1,i}\left[\frac{\partial}{\partial r}(C_{1,i}) + \frac{C_{1,i}}{RT}\left(\bar{V}_{1,i} - \frac{M_i}{\rho_i}\right)\frac{\partial}{\partial r}(\sigma_{h,i})\right] \quad i = p, n \qquad [8]$$

and the governing equation for diffusion in the particle is modified as follows

$$\frac{\partial C_{1,i}}{\partial t} = \frac{1}{r^2}\frac{\partial}{\partial r}\left\{D_{1,i}\left[r^2\frac{\partial C_{1,i}}{\partial r} + \frac{C_{1,i}}{RT}\left(\bar{V}_{1,i} - \frac{M_i}{\rho_i}\right)r^2\frac{\partial \sigma_{h,i}}{\partial r}\right]\right\} \quad i = p, n \qquad [9]$$

Equation 9 has been derived from the generalized Maxwell–Stefan equation based on the assumptions that the particle is isothermal and that lithium and the host form an ideal binary mixture.

This equation is a valid representation of the scenario wherein diffusion takes place in a material comprised of a single homogeneous phase. Most of the intercalation electrode materials, such as Li_xCoO_2 and carbon, are comprised of two or more coexisting phases during certain stages of the intercalation process.[22,23] Diffusion occurs at different rates in all these phases, and there is a sharp difference in composition at the phase interface. In addition to this fact, the phases can have different structural and mechanical properties leading to a discontinuity in the driving force due to the hydrostatic stress (pressure) at the phase interface. To properly account for the phase transformation process and diffusion within each of the phases, it is necessary to know the criteria for the initiation of the different phases and to track the movement of the phase interface in the material. To achieve this goal, the moving boundary approach presented by Zhang and White[24] is used.

Moving boundary model.— The framework presented in Ref. 24 to account for diffusion in the coexisting phases in the electrode particle is revisited and modified to include the effect of stress on the diffusion process. During the intercalation/deintercalation process of lithium into the electrode, a series of phase transformations takes place which is commonly referred to as staging phenomena. For certain ranges of composition, two of the transforming phases coexist in the material. For example, in Li_xCoO_2, when the lithium concentration (x in Li_xCoO_2) is between 0.75 and 0.97, two phases coexist.

In this study the coexisting phases in the electrodes are considered to be in equilibrium with each other, and the phases are referred to as α and β, respectively. The α phase refers to the lithium deficient phase and the β phase refers to the lithium rich phase in the electrode. Diffusion of lithium occurs in both of phases and diffusion inside the two phases is described using two separate governing equations. Diffusion equations including the effect of stress for each of the two phases α and β are, respectively, given by

$$\frac{\partial C_{1,i}^{\alpha}}{\partial t} = \frac{1}{r^2}\frac{\partial}{\partial r}\left\{D_{1,i}^{\alpha}\left[r^2\frac{\partial C_{1,i}^{\alpha}}{\partial r} + \frac{C_{1,i}^{\alpha}}{RT}\left(\bar{V}_{1,i}^{\alpha} - \frac{M_i}{\rho_i}\right)r^2\frac{\partial \sigma_{h,i}^{\alpha}}{\partial r}\right]\right\} \quad i = p, n \qquad [10]$$

$$\frac{\partial C_{1,i}^{\beta}}{\partial t} = \frac{1}{r^2}\frac{\partial}{\partial r}\left\{ D_{1,i}^{\beta}\left[r^2 \frac{\partial C_{1,i}^{\beta}}{\partial r} + \frac{C_{1,i}^{\beta}}{RT}\left(\bar{V}_{1,i}^{\beta} - \frac{M_i}{\rho_i} \right) r^2 \frac{\partial \sigma_{h,i}^{\beta}}{\partial r} \right] \right\} \quad i = p,\ n \qquad [11]$$

where $C_{1,i}^{\alpha}$ and $C_{1,i}^{\beta}$ are the concentrations of lithium in α and β phases of the electrode, respectively, and $\bar{V}_{1,i}^{j}$ is the partial molar volume of phase j in the electrodes. The movement of the phase boundary is assumed to be controlled by the diffusion process in the adjacent phases, and the governing equation used to track the position of the interface, i.e., the velocity of the phase boundary movement, is given by a jump material balance[20] at the interface as follows

$$(C_{eq,i}^{\alpha} - C_{eq,i}^{\beta})\frac{dr_i}{dt} = D_{1,i}^{\alpha}\frac{\partial C_{1,i}^{\alpha}}{\partial r} - D_{1,i}^{\beta}\frac{\partial C_{1,i}^{\beta}}{\partial r} \quad i = p,\ n \qquad [12]$$

where $C_{eq,i}^{\alpha}$ and $C_{eq,i}^{\beta}$ are the maximum soluble concentrations of lithium in α and β phases of the electrode, respectively.

The electrochemical reaction occurs at the particle/electrolyte interface and lithium diffuses through the phase present near the surface (the β phase is formed at the surface during intercalation and the α phase is formed at the surface during deintercalation). The lithium flux at the particle surface is given by

$$-D_{1,i}^{j}\frac{\partial C_{1,i}^{j}}{\partial r}\bigg|_{r=R_i} = \frac{J_i}{a_i F}, \quad i = p,\ n\ ; \quad j = \alpha/\beta \qquad [13]$$

Equations10-13 form the set of equations to describe diffusion inside the electrode particles during phase transformation. Equations 10 and 11 are used to describe the diffusion process in α and β phases, respectively, during a single phase regime, along with the appropriate boundary condition described in Eq. 13.

The hydrostatic stress σ_h mentioned in the diffusion equations as one of the driving forces (see Eq. 9-11) is the average of the three principal components of the stress tensor and for a spherical particle, it can be expressed as shown below[21]

$$\sigma_h = \frac{\sigma_r + 2\sigma_t}{3} \qquad [14]$$

where σ_r and σ_t are the radial and tangential components of the stress tensor, respectively. Governing equations describing these stress components in the electrode are described in the following section.

Mechanical stress.— To quantify the stress generated in the electrode, the elastic deformation of the material must be related to the intercalation process. The stress arising due to the diffusion process is modeled using an approach similar to that used to account for thermally induced stress in a material.[21] A similar methodology has been used in the past while estimating stress in the intercalation electrode materials.[12,14,15] To formulate the equations describing stress distribution in the intercalation particles, the following assumptions are made: (*i*) mechanical properties are assumed to be constant within each phase of the intercalation material, (*ii*) the material is assumed to be completely elastic until failure, and (*iii*) mechanical equilibrium is assumed to exist within the material. The equation of momentum describing the motion of each point inside the spherical particle, which is in mechanical equilibrium, is written in terms of the principal components of the stress tensor as follows[21]

$$\frac{\partial \sigma_{r,i}^{j}}{\partial r} + \frac{2}{r}(\sigma_{r,i} - \sigma_{t,i}) = 0, \quad i = p,\ n\ ; \quad j = \alpha,\ \beta \qquad [15]$$

where $\sigma_{r,i}$ and $\sigma_{t,i}$ are the radial and tangential components of the stress tensor in region i and these can be expressed in terms of the radial displacement (u_i) in region i and mechanical properties for materials as follows[21]

$$\sigma_{r,i}^{j} = \frac{E_i^j}{(1+\nu_i^j)(1-2\nu_i^j)}\left[(1-\nu_i^j)\frac{\partial u_i}{\partial r} + 2\nu_i^j \frac{u_i}{r} - (1+\nu_i^j)\Omega_i^j C_{1,i}^j \right], \quad i = p,\ n\ ; \quad j = \alpha,\ \beta \qquad [16]$$

$$\sigma_{t,i}^{j} = \frac{E_i^j}{(1+\nu_i^j)(1-2\nu_i^j)}\left[\nu_i^j \frac{\partial u_i^j}{\partial r} + \frac{u_i^j}{r} - (1+\nu_i^j)\Omega_i^j C_{1,i}^j \right], \quad i = p,\ n\ ; \quad j = \alpha,\ \beta \qquad [17]$$

where E_i^j is Young's modulus of elasticity for the material in phase j and region i, ν_i^j is Poisson's ratio, and Ω_i^j is the expansion coefficient due to intercalation which is equivalent to $\bar{V}_i^j/3$, where $\bar{V}_i^j$ is the partial molar volume of phase j in region i.

Equations 10-13 and 15 form the set of governing equations describing diffusion and stress generation in the solid phase of each of the electrodes. These equations are coupled with the governing equations for solid and solution phase potentials (Eq. 1 and 2) and solution phase concentration (Eq. 3). The numerical solution procedure is described in detail in the following section.

Solution Procedure

The numerical simulations were carried out using COMSOL Multiphysics,[25] a simulation package that uses the finite element method to discretize the governing equations.

Discretization scheme.— Each model region (positive electrode, separator, and negative electrode) is discretized along the *x* coordinate. Solution phase potential ϕ_2 and solution phase concentration C_2 are the variables solved for in all three regions, and solid phase potential ϕ_1 is solved in positive and negative electrodes only. To evaluate the kinetic expression in the electrodes, the concentration of lithium is required at the local particle/electrolyte interface throughout the length of the positive and negative electrodes. To accomplish this goal and to estimate the stresses inside the particles, Eq. 11-14 and 16 is solved in the spatial *r* direction at each node point along the *x* coordinate in the electrodes. The radial coordinate *r* is scaled using the following expression to avoid any convergence issues arising due to the difference in the length scales between the macroscopic length of the electrode (*x* coordinate) and the radius of the particles (*r* coordinate)[19]

$$y = \frac{rL_i}{R_{1,i}}\ ; \quad i = p,\ n \qquad [18]$$

Moving mesh within the electrode.— Due to the phase boundary movement in the positive electrode, the mesh points are not fixed. Studies in the past have made use of different numerical methods to handle the moving boundaries. Some of these include fixed mesh/grid methods using implicit or explicit finite difference approximations, moving mesh methods using either variable time step or variable space intervals and coordinate transformations. A detailed review of these schemes can be found elsewhere.[26] In this study the moving mesh method available in COMSOL Multiphysics simulation package is used for framing the set of moving boundary equations in the positive electrode. This scheme makes use of the Arbitrary Lagrangian–Eulerian (ALE) formulation which makes it possible to solve the diffusion and stress equations and the moving boundary equation simultaneously.

Coupled model.— The concentration and stress equations in both positive and negative electrodes are highly coupled with the porous electrode equations. All of these equations are solved simultaneously. At any given time, the set of variables solved for are {ϕ_1, ϕ_2, C_2, $C_{1,n}$, σ_n, $C_{1,p}^{\alpha}/C_{1,p}^{\alpha}$, and $\sigma_p^{\alpha}/\sigma_p^{\beta}$} or {$\phi_1$, ϕ_2, C_2, $C_{1,n}$, σ_n, $C_{1,p}^{\alpha}$, $C_{1,p}^{\alpha}$, σ_p^{α}, and σ_p^{β}} based on whether a single or two phase exists in the positive electrode, respectively.

Table I. List of parameter values used in the model.

Parameters	Value			Reference
		Electrode parameters		
	$LiCoO_2$		LiC_6	
	α phase	β phase		
C_1^{max} (mol/cm^3)	$49{,}943 \times 10^{-6}$	$49{,}943 \times 10^{-6}$	$31{,}858 \times 10^{-6}$	27
D_1 (cm^2/s)	1×10^{-9}	2×10^{-10} [a]	$1.4523 \times 10^{-9} \exp\left[\frac{68{,}025.7}{R}\left(\frac{1}{318} - \frac{1}{T}\right)\right]$	24
E (GPa)	70	70	15[c]	[b]
$\bar{V}^* = (\bar{V})/(M/\rho)$	0.985	0.9999	1.103[c]	28
ν	0.2	0.16	0.3[c]	28
M (g/mol)	97.8		78.64	31
ρ (g/cm^3)	5.03		2.2	6
σ (S/cm)	0.1		1	27
		Thermodynamic and kinetic parameters		
α	0.5		0.5	27
k [A/cm^2/(mol/cm^3)$^{1.5}$]	0.127	0.243	0.101	[a]
		Design adjustable, solution phase, and other parameters		
	$LiCoO_2$	Separator	LiC_6	
R_1 (μm)	8.5	—	12.5	27
ε_1	0.55	—	0.5052	27
ε_2	0.3	0.45	0.4382	27
L (μm)	70	25	73.5	27
Brug	1.5	1.5	1.5	[a]
t^+	0.363			24
C_2^0 (mol/cm^3)	1000×10^{-6}			27
D_2 (cm^2/s)	See Eq. A-7			24
κ	See Eq. A-3			24
F (As/mol)	96,487			31
T (K)	298			[d]
R (J/mol K)	8.314			31

[a] Values fit to experimental data.
[b] Assumed.
[c] Reference 12.
[d] Operating condition.

Parameters.— The list of design and other parameters used in the simulations is provided in Table I. The open-circuit potential data for Li_xCoO_2 and carbon were obtained from the experimental work conducted by Kumaresan et al.[27] Poisson's ratio for Li_xCoO_2 was calculated from the change in the lattice parameters reported in Ref. 28. Young's modulus E for $LiCoO_2$ is not available in the literature and hence we chose to use the value of E of lithium aluminum silicate, which has a similar lattice structure, trigonal with the $R\bar{3}m$ space group. The partial molar volume of Li_xCoO_2 was calculated from the change in lattice volume with change in lithium concentration, as reported by Reimers and Dahn.[28] All the mechanical properties of carbon electrode used were obtained from Ref. 12.

Results and Discussion

The simulation results for the positive electrode are presented and discussed first, and the results for the negative electrode are discussed in a subsequent section.

Positive electrode ($LiCoO_2$).— For illustration purposes, the results described in the following sections consider the phase changes within the cathode only. The stresses in the $LiCoO_2$ electrode result from two processes. The intercalation or de-intercalation process leads to a change in lattice volume of the crystal in the single phase region, leading to stress. This stress is referred to as intercalation induced stress or intercalation stress. Another origin of the stress in

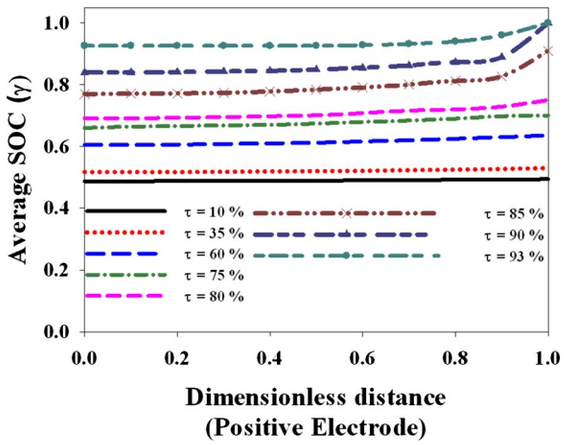

Figure 2. (Color online) Average SOC of the particles across the thickness of the positive electrode (C/2).

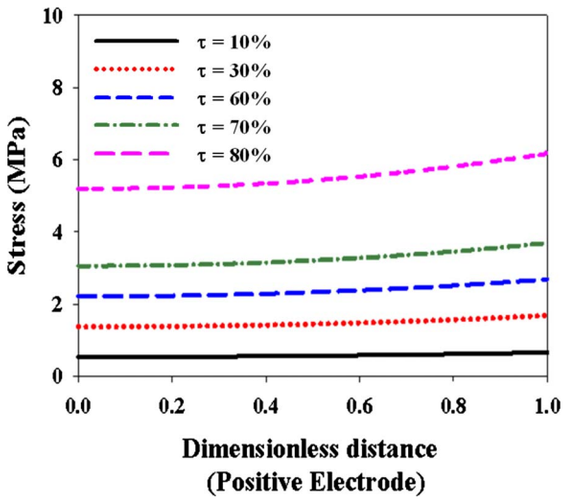

Figure 3. (Color online) Intercalation stresses at the surface of the particles across the thickness of the positive electrode during discharge (C/2).

the electrode particle is the phase transformation occurring over a range of lithium concentrations (0.75–0.97). This stress is referred to as phase transformation induced stress or phase transformation stress. Both these stresses are the functions of SOC. Here the SOC in the electrode particle γ is defined as the ratio of average concentration of lithium in the particle to the maximum possible concentration of lithium in the particle

$$\gamma = \frac{\bar{C}_{1,i}}{C_{1,i}^{max}}, \quad i = p \qquad [19]$$

Figure 2 shows the average local SOC γ of the particles along the thickness in the electrode as a function of τ for a discharge rate of C/2. Here τ is expressed as the SOC of the positive electrode normalized to the maximum SOC of the positive electrode at the end of a low rate discharge (C/33)

$$\tau = \left[\int_i \gamma\right]_m \Big/ \left[\int_i \gamma^{max}\right]_{C/33}$$

$$i = p \quad m = \text{given rate of discharge} \qquad [20]$$

To understand the diffusion and phase transformation processes occurring in the electrode and to correlate the stresses arising in the electrode to the individual process, the plots in Fig. 2 are conveniently divided into three groups based on the value of τ. In the first regime ($\tau < 80\%$) all the particles across the electrode are comprised of single α phase. In this regime the γ increases uniformly across the thickness of the electrode (here the dimensionless x coordinate equals 0 represents the current collector and 1 denotes the separator) with a corresponding increase in τ as a result of diffusion of lithium into the particles.

When $\tau = 80\%$, the surface concentration of lithium in the particles close to the separator ($x = 1$) reaches the equilibrium concentration (C_{eq}^{α}), and the phase transformation is initiated in those particles. In the regime when $80\% < \tau < 85\%$, there is a mixture of single and two phase particles in the electrode, particles that are close to the separator have two phases (α,β) and the rest of the particles have a single phase (α). The second phase formed (β) has a higher soluble concentration ($C_{eq}^{\beta} = 0.97$); therefore the average SOC (γ) increases rapidly in the particles that have undergone phase transformation compared to particles having only α phase. With a further increase in τ ($\tau > 85\%$), the phase transformation front moves back into the electrode toward the current collector. In this regime all the particles have two phases, and the value of γ depends on the extent of phase transformation in the particle.

In the first regime ($\tau < 80\%$), when the whole electrode is comprised of a single phase, the particles experience only intercalation induced stress. Figure 3 shows the magnitude of the intercalation stress at the surface of the particle as a function of τ for a discharge rate of C/2. From Fig. 2 and 3 it can be observed that stress in the single phase regime increases monotonously with an increase in γ of the particles in the electrode. The simulation results indicate (Fig. 3) that the magnitude of the intercalation stress in the single phase regime is larger in the particles close to the separator end than the particles elsewhere in the electrode. This is expected because the γ is higher in the particles close to the separator during the discharge process. As the reaction zone moves gradually into the electrode toward the current collector, γ and stress in the particles in those regions start to increase. From Fig. 3 the magnitude of the stress is maximum at $\tau = 80\%$ in the particle close to the separator. At this point the phase transformation starts and the stress starts to decrease in those particles.

In the mixed regime when $80\% \leq \tau < 85\%$, particles that have undergone phase transformation experience both intercalation and phase transformation stresses, while the rest of the particles still experience only intercalation stress. In the third regime ($\tau > 85\%$), all the particles experience both the stresses. Figure 4a and b depicts the differential stresses at the phase interface in the particles along the thickness of the electrode as a function of τ (both for regimes 2 and 3) for discharge rates of C/2 and C/33, respectively. In the region of the electrode where the phase transformation has not been initiated (for regime 2), the differential stress actually refers to the single phase (α) intercalation stress.

In the particles with two phases, both phases have different values of the partial molar volume,[28] and they experience different extents of expansion/contraction during the intercalation of lithium. Lithium deficient core (α phase) has a larger partial molar volume than the lithium rich shell region (β phase) of the particle. Therefore as the second phase (β) starts to form during the discharge process, the magnitude of stress starts to decrease. This trend is true for materials such as Li_xCoO_2 whose lithium rich phase has a lower partial molar volume. The trend reverses for materials that expand upon lithium intercalation and whose β phase has a higher partial molar volume than α phase.

In addition to the different values of partial molar volume, both phases have different lattice parameters and hence different mechanical properties (i.e., Poisson's ratio). The abrupt change in the lattice parameters at the phase boundary leads to a differential strain (misfit strain) at the interface. To maintain a coherent interface, the

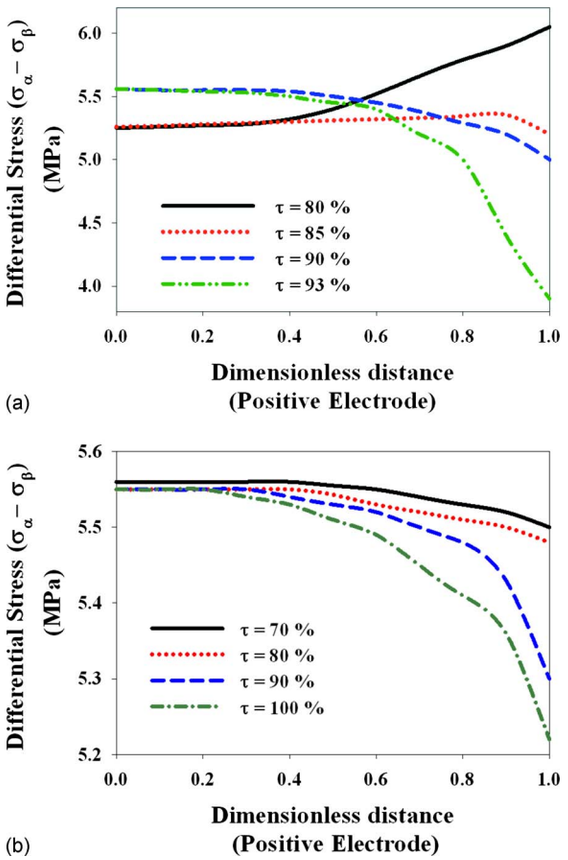

Figure 4. (Color online) (a) The differential stress between two phases inside the particles along the thickness of the positive electrode during discharge (C/2). (b) The differential stress between two phases inside the particles along the thickness of the positive electrode during discharge (C/33).

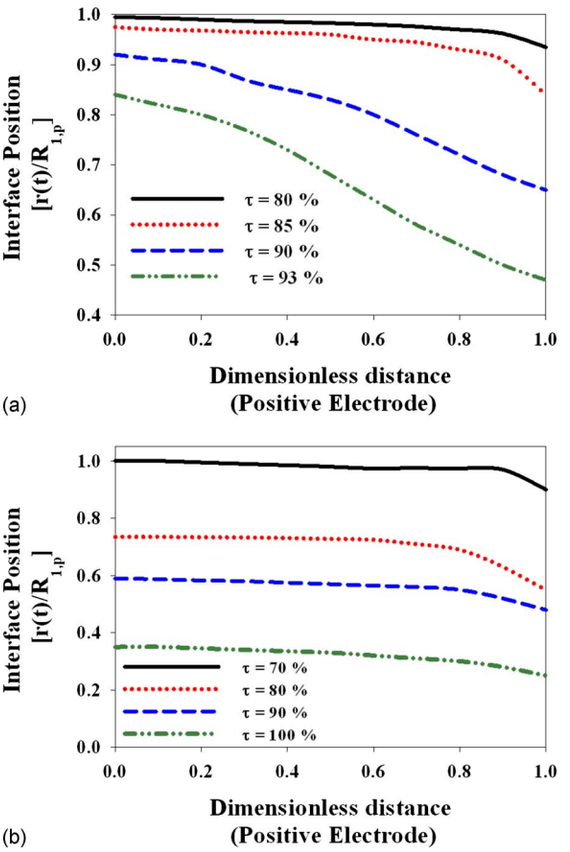

Figure 5. (Color online) (a) Position of the phase interface inside the particles along the thickness of the positive electrode during discharge (C/2) and (b) position of the phase interface inside the particles along the thickness of the positive electrode during discharge (C/33).

misfit strain has to generate a differential stress across the interface. The spherical symmetry of the particle forces the strain (and also stress) in the radial direction to be a continuous function across the phase boundary. The misfit strain is experienced in the tangential direction, giving rise to a differential stress (tangential component) at the phase boundary inside the particle. The distribution of this stress across the electrode closely follows the phase transformation in the individual particles.

Figure 5a and b depicts the extent of the phase transformation as a function of τ in the particles across the thickness of the positive electrode for discharge rates of C/2 and C/33, respectively. The phase transformation is initiated at the separator end of the electrode and propagates across the electrode toward the current collector. From these results (Fig. 2-5) it can be summarized that the evolution of stress in the particles along the thickness of the electrode at any given time during discharge depends both on the extent of intercalation and phase transformation in the individual particles at that time.

The intercalation induced stress increases with an increase in the rate of discharge process. This is illustrated in Fig. 6, which is a plot of the maximum value of stress generated in the particles during the discharge process as a function of the rate of discharge. In the simulations considered in this study, the maximum values of stress obtained in all these simulation scenarios are at the particle close to the separator toward the end of the single phase regime (regime 1). The phase transformation stress does not seem to have a direct dependency on the rate of discharge, but depends on the extent of phase transformation. The maximum differential strain (expressed as the percent change in tangential strain) at the phase boundary, which is plotted as a function of the rate of discharge (see Fig. 6), increases with an increase in the rate of discharge until a certain rate (C/2 in this study), and then starts to decrease with an increase in the rate of discharge. The differential strain is proportional to the relative displacement of the two phases at the phase boundary, which in turn depends on the concentration of the two phases present within the particle. When the amount of the β phase increases, the α phase in the core does not have to contract much at the interface to accommodate the β phase.[10] At low rates of discharge the extent of phase transformation is higher and therefore the strain experienced at the

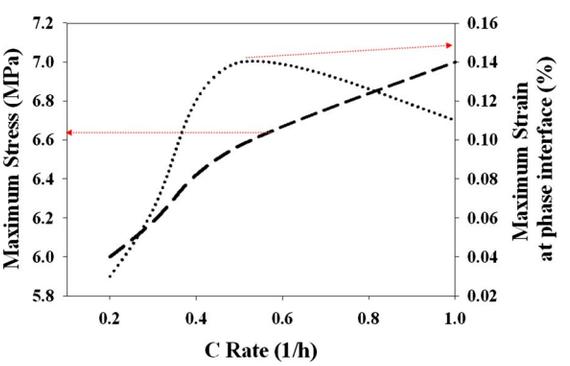

Figure 6. (Color online) Effect of discharge rate on (left axis) maximum intercalation stress in the positive electrode and (right axis) maximum differential strain at the phase interface.

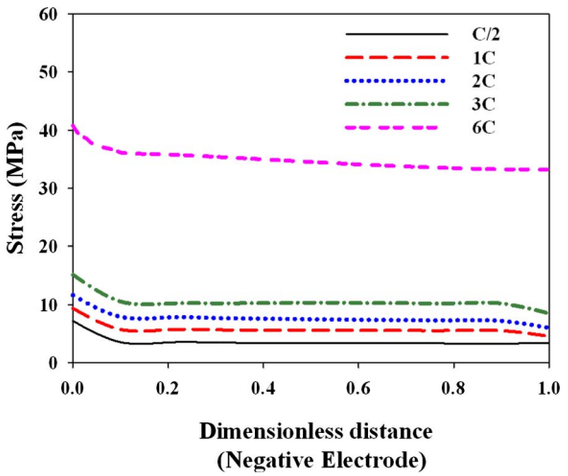

Figure 7. (Color online) Total stress at the surface of the particles along the thickness of the anode for different rates of discharge.

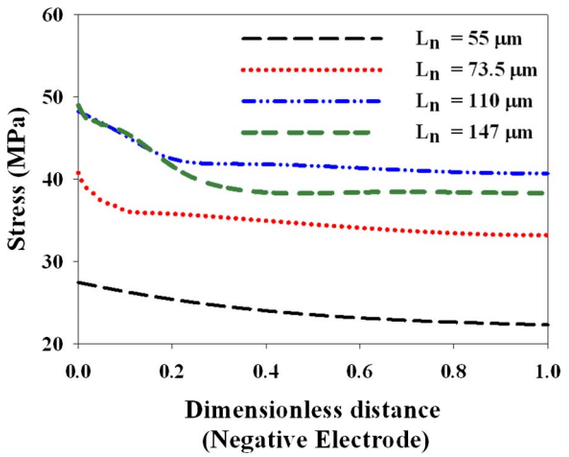

Figure 8. (Color online) Total stress at the surface of the particles along the thickness of the anode for various thickness values.

interface is less. At very high rates of discharge, the amount of phase transformation is not significant enough to cause a relative displacement at the interface. These two counteracting effects lead to the pattern observed in Fig. 6 for maximum differential strain obtained at various rates of discharge.

The magnitudes of intercalation stresses observed in the positive electrode for all cases shown in Fig. 2 and 4 are less than the yield stress of the material which is assumed to be the yield strength of lithium aluminum silicate (~100 MPa). Hence, a fracture or crack in the material due to this stress is not predicted. The intercalation stress, being a function of lithium concentration, is reversible during cycling; hence the effects of residual stress or fatigue would be insignificant in the material investigated. The phase transformation induced strain at the interface depends on the extent of the transformation. Cycling of the cell may lead to different extents of phase transformation within the electrode at each charge/discharge cycle. The fluctuation in the extent of phase transformation leads to the buildup of residual strain in the particles over an extended period of cycling, and the buildup of residual strain in the material may lead to the loss in performance, unless the strain is relieved by mechanisms such as incoherent phase transformation or fracture.[29] In most ceramic materials such as $LiCoO_2$, the critical strain needed to cause fracture is typically in the order of 1%.[30] Hence an electrode having particles of size similar to the one used in this study can experience severe damage when cycled at intermediate rates (i.e., C/2 or 1C) over an extended period of time such as those observed in the study reported in Ref. 8. The actual life of the electrode depends on the operating conditions such as temperature, depth of discharge, size of the particles, and other design parameters. Prediction of cell performance during cycling is the subject of a different study.

Negative electrode (carbon).— Figure 7 depicts the stress distribution at the local particle surface across the thickness of the negative electrode at the end of the discharge for various discharge rates. The magnitude of stress is relatively higher in the particles closer to the separator ($x = 0$) than in the particles near the current collector ($x = 1$). The magnitude of stress within the electrode increases with rates of discharge. At lower rates, the utilization of particles is more or less uniform across the electrode thickness, therefore leading to a relatively uniform stress distribution across the thickness than at higher rates such as 6C. The simulated results also predict that at the 6C rate of discharge, the particles closer to the separator experience stress values higher than the tensile yield strength of carbon (30 MPa). Therefore these particles have a higher tendency to develop microcracks or fracture. The choice of design parameters such as thickness, porosity, and particle size affects the magnitude of stress and hence the life of the negative electrode. In this study the simulations were performed by varying the thickness, porosity, and particle size of the negative electrode, while holding constant the capacity ratio of the positive/negative electrode (0.925).

The impact of thickness of the negative electrode on the magnitude of stress generated in the electrode is illustrated in Fig. 8. All the other parameters and design variables are the same as in the base case (see Table I), except for positive and negative electrode thicknesses. To maintain the positive/negative electrode capacity ratio, with a change in the negative electrode thickness, a corresponding change is made to the positive electrode thickness. Four different negative electrode thicknesses are considered including the base case parameter, and these case scenarios will be referred to as cases 8a, 8b, 8c, and 8d, respectively, in the order of increasing thickness. The rate of discharge is 6C. Here the "C rate" refers to the ratio of apparent current density and the capacity of the electrode. With an increase in the thickness of the electrode, there is a corresponding increase in the capacity of the electrode and hence at any particular rate, the apparent current density is also increased.

The general trend found in the base case scenario (Fig. 7) for the stress distribution across the thickness is also found for all the other cases. In all the cases considered in this study, the magnitude of stress is higher at the separator end of the negative electrode and decreases toward the current collector. As the thickness of the electrode is increased, the stress is increased as well. This is because of the fact that as the thickness of the electrode is increased, the cell capacity (and hence the apparent current density or reaction rate experienced by the particles) is increased. Beyond a certain thickness value, for instance, case 7d in this study, the particles toward the current collector experience much less current density than the average electrode due to the liquid phase limitations in the electrode. Therefore the stress decreases rapidly across the thickness, and the magnitude of stress obtained near the current collector for case 8d is less than the stress obtained for case 8c (comparatively thinner electrode).

From these results (Fig. 8) it can be concluded that for a given rate of discharge, a thicker electrode not only reduces the performance of the battery operated at high rates of discharge but also experiences increased stresses. An optimized electrode thickness to obtain the desired power density improves both the performance and life of the battery electrodes.

Figure 9 shows the effect of porosity in the negative electrode on the generation of stress in the electrode. As in the previous simulation, the positive/negative electrode capacity ratio is held constant in this case as well. Three different negative electrode porosities including the base case parameter are considered, and these case scenarios will be referred to as cases 9a, 9b, and 9c, respectively, in the

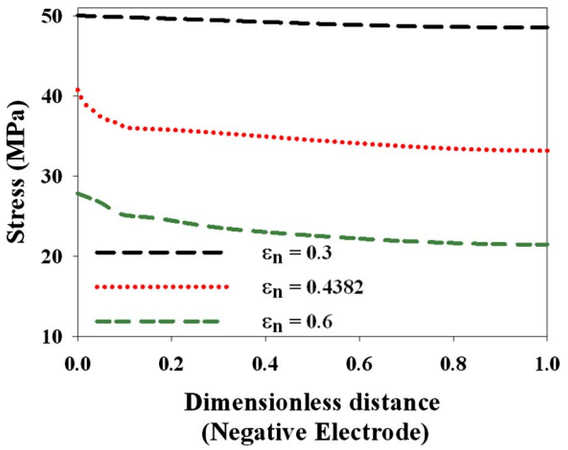

Figure 9. (Color online) Total stress at the surface of the particles along the thickness of the anode for various porosity values.

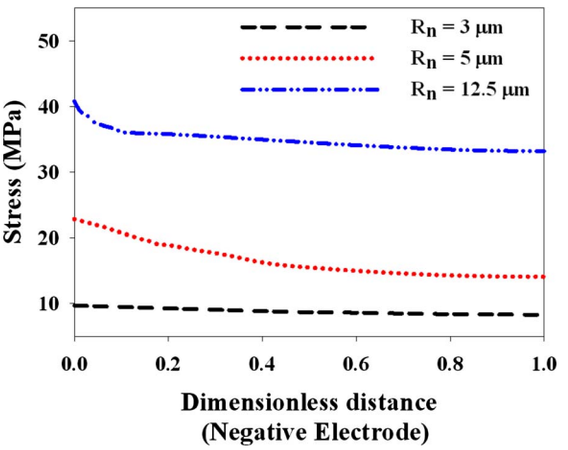

Figure 10. (Color online) Total stress at the surface of the particles along the thickness of the anode for various particle sizes.

order of increasing porosity. Figure 9 shows that as the porosity is increased, the magnitude of stress decreases for a given rate of discharge. With an increase in porosity in the electrode capacity, the apparent current density experienced by the particles decreases and thereby the magnitude of stress generated decreases. When the porosity is decreased (see case c in Fig. 9), stress distribution is rather uniform throughout the thickness of the electrode. This is contrary to the scenario of an increase in thickness (case d in Fig. 8) wherein the stress in the particles close to the separator was more pronounced than the stress in the particles elsewhere in the electrode. From Fig. 9 it can be concluded that a decrease in porosity of the electrode is more detrimental to the mechanical life of the electrode than increasing the thickness of the electrode. These results not only highlight the importance of choosing optimum design porosity but also indicate that the mechanical stress in the negative electrode can increase if there is a significant decrease in the porosity during the operation of the battery (assuming identical physical properties for the side reaction products blocking the pores). It has been widely accepted in the literature[4-6] that the porosity in fact decreases in the negative electrode during the operation of the battery due to various side reaction products. This decrease in porosity in the electrode decreases both the performance and more significantly the mechanical life of the electrode. It has been reported in the study by Kostecki and McLarnon that structural damage increases the amount of side reaction product.[9] These results and the results predicted in the present study underscore the importance of mutual effects of these two failure modes, each enhancing the other and leading to a vicious cycle of damage and ultimate failure of the battery electrode.

The third scenario considered in this study was to understand the effect of particle size on the magnitude of stress in the electrode. Three different particle sizes are considered. Results for this set of simulations are presented in Fig. 10. It can be observed that a decrease in particle size decreases the magnitude of stress significantly. Very small particles have a larger surface area and a high side reaction rate. This aspect is not considered in this study. Of all the design parameters considered in this study, the particle size has the most significant influence on the magnitude of overall stress generation in the electrode. An electrode with smaller particles with optimum thickness and porosity for the desired application not only enhance the life of the battery but improve the performance of the battery.

Conclusions

A comprehensive model was developed to understand the stress generation in porous intercalation electrodes during the discharge process in a lithium ion cell. The process of phase transformation and stress generated as a result of the process was considered for the positive electrode (lithium cobalt oxide). The intercalation stress increased with the rate of discharge, and the phase transformation stress depended on the amount of each phase present in the electrode. The results from the simulation indicate that the particles that are cycled over an extended period at intermediate or even low rates of discharge can be damaged due to the residual strain buildup caused by phase transformation in the material. The magnitude of stress generated in the negative electrode (carbon) was much higher compared to that of the positive electrode. The simulations conducted in this study also indicated high probability of fracture or mechanical damage in the particles close to the separator in the negative electrode. Simulations were conducted with different thicknesses, porosities, and particle sizes in the negative electrode. The overall magnitude of stress decreased during the discharge process with a decrease in thickness, a decrease in particle size, and an increase in porosity. The size of the particles in the electrode had a higher impact in reducing the stress generation than the thickness and the porosity in the simulations performed in this study. A complete investigation of the phase changes within the negative electrode should consider staging of the active material during the intercalation process,[23,32] and the treatment of the stress buildup during this complicated phenomenon is the subject of a separate study. While the results presented here generally agree with experimental observations, quantifying stress distribution within electrodes experimentally is an essential step toward designing better electrodes, and significant efforts have gone toward such measurements.[7-9,32-35]

Acknowledgment

The authors are grateful for the financial support of this project provided by the National Reconnaissance Office (NRO) under contract no. NRO-000-03-C-0122.

University of South Carolina assisted in meeting the publication costs of this article.

List of Symbols

a	specific interfacial area of the electrode, cm^2/cm^3
brug	Bruggemann's exponent factor
C_1	concentration of lithium in the solid phase, mol/cm^3
C_2	concentration of lithium ion in the electrolyte, mol/cm^3
$C_{1,0}$	stress-free lithium concentration (concentration at the fully charged state) in the solid phase, mol/cm^3
$\bar{C}_1$	average concentration of lithium in particle, mol/cm^3
C^{max}	maximum stoichiometric concentration of lithium at the particle surface, mol/cm^3
C_1^S	concentration of lithium at the surface of the particle, mol/cm^3
D^{eff}	effective diffusion coefficient of lithium in the particle including the effect of stress, cm^2/s
D_1	diffusion coefficient of lithium in the solid phase, cm^2/s

D_2	diffusion coefficient of lithium in the solution phase, cm^2/s
E	Young's modulus, N/cm^2
F	Faraday's constant, 96,487, C/mol
i_o	exchange current density for the electrochemical reaction, A/cm^2
I^{app}	applied current, A
j	rate of the electrochemical reaction at the particle surface, mol/cm^2 s
k	reaction rate constant, $(A/cm^2)/(mol/cm^3)^{1.5}$
M	molecular mass, g/mol
$\hat{n}$	normal component to the surface
r	radial coordinate, C m
R	gas constant, 8.314, J/mol K
R_p	radius of the particle, C m
t^+	transference number
t	time, s
T	temperature, K
u	displacement vector, C m
U^{ref}	open-circuit potential, V
V	cell potential, V
$\bar{V}_{Li}$	partial molar volume of lithium in the intercalation material, cm^3/mol
x	spatial coordinate along the thickness of the cell, C m
y	scaled radial coordinate, C m

Greek

α_i	transfer coefficient of the electrochemical reaction in region i
γ	average SOC of the particle
ε_1	volume fraction of the active material
ε_2	porosity of the electrode
η	overpotential driving the electrochemical reaction, V
κ	conductivity of solution phase, S/cm
κ_D	diffusional conductivity, S/cm
ν	Poisson's ratio
ρ	density of the particle, g/cm^3
σ	conductivity of solid phase, S/cm
σ_h	hydrostatic stress, N/cm^2
σ_r	radial component of stress, N/cm^2
σ_t	tangential component of stress, N/cm^2
τ	SOC of positive electrode, %
ϕ_1	solid phase potential, V
ϕ_2	solution phase potential, V

Subscript

i	region of the cell (=n or p)
m	rate of discharge
n	negative electrode
p	positive electrode
r	radial
s	separator
t	tangential

Superscript

app	applied
eff	effective
j	phase in the material
max	maximum
S	surface of the particle
α	alpha phase
β	beta phase

Appendix

This appendix lists the solid phase and electrolyte properties used in the simulation. The effective conductivities (in S/cm) of solid and solution phases, respectively, are

$$\sigma_i^{eff} = \sigma_i \varepsilon_{1,i} \quad i = p,n \qquad [A\text{-}1]$$

$$\kappa^{eff} = \kappa \varepsilon_2^{brug} \qquad [A\text{-}2]$$

where the solution phase conductivity (in S/cm) is given by[27]

$$\kappa = C_2(-10.5 + 0.074T - 6.96 \times 10^{-5}T^2 + 668C_2 - 17.8C_2T + 0.028C_2T^2 + 4.94 \times 10^5 C_2^2 - 886C_2^2T)^2 \qquad [A\text{-}3]$$

The diffusional conductivity is given by

$$\kappa_D = -\frac{2RT\kappa^{eff}}{F}\upsilon \qquad [A\text{-}4]$$

where the thermodynamic factor, which accounts for the nonideality of the electrolyte at room temperature, is given by[27]

$$\upsilon = (1 - t^+)\left(1 + \frac{d \ln f_{\pm}}{d \ln C_2}\right) = 1.639 - 0.655C_2^{0.5} + 43{,}082.9C_2^{1.5} \qquad [A\text{-}5]$$

The effective diffusion coefficient of the electrolyte (in cm^2/s) is given by

$$D_2^{eff} = D_2 \varepsilon_2^{brug} \qquad [A\text{-}6]$$

where the diffusion coefficient is given by[27]

$$\log(D_2) = -4.43 - \frac{54}{T - 5 \times 10^3 C_2 - 229} - 2.2 \times 10^2 C_2 \qquad [A\text{-}7]$$

References

1. S. G. Chalk and J. F. Miller, *J. Power Sources*, **159**, 73 (2006).
2. G. H. Kim, A. Pesaran, and R. Spotnitz, *J. Power Sources*, **170**, 476 (2007).
3. P. Arora, M. Doyle, and R. E. White, *J. Electrochem. Soc.*, **146**, 3543 (1999).
4. G. Sikha, B. N. Popov, and R. E. White, *J. Electrochem. Soc.*, **151**, A1104 (2004).
5. R. Darling and J. Newman, *J. Electrochem. Soc.*, **145**, 990 (1998).
6. P. Ramadass, B. Haran, P. M. Gomadam, R. E. White, and B. N. Popov, *J. Electrochem. Soc.*, **151**, A196 (2004).
7. E. Markervich, G. Salitra, M. D. Levi, and D. Aurbach, *J. Power Sources*, **146**, 146 (2005).
8. H. Wang, Y. Jang, B. Huang, D. R. Sadoway, and Y. M. Chiang, *J. Electrochem. Soc.*, **146**, 473 (1999).
9. R. Kostecki and F. McLarnon, *J. Power Sources*, **119–121**, 550 (2003).
10. J. Christensen and J. Newman, *J. Electrochem. Soc.*, **153**, A1019 (2006).
11. X. Zhang, W. Shyy, and A. M. Sastry, *J. Electrochem. Soc.*, **154**, A910 (2007).
12. J. Christensen and J. Newman, *J. Solid State Electrochem.*, **10**, 293 (2006).
13. X. Zhang, A. M. Sastry, and W. Shyy, *J. Electrochem. Soc.*, **155**, A542 (2008).
14. Y. T. Cheng and M. W. Verbrugge, *J. Power Sources*, **190**, 453 (2009).
15. R. E. Garcia, Y. M. Chiang, W. C. Carter, P. Limthongkul, and C. M. Bishop, *J. Electrochem. Soc.*, **152**, A255 (2005).
16. M. Doyle, T. F. Fuller, and J. Newman, *J. Electrochem. Soc.*, **140**, 1526 (1993).
17. T. F. Fuller, M. Doyle, and J. Newman, *J. Electrochem. Soc.*, **141**, 1 (1994).
18. J. S. Newman and K. E. Thomas-Alyea, *Electrochemical Systems*, 3rd ed., Prentice-Hall, Englewood Cliffs, NJ (2004).
19. P. Ramadass, Ph.D. Thesis, University of South Carolina, Columbia, SC (2003).
20. J. C. Slattery, *Advanced Transport Phenomena*, Cambridge University Press, New York (1999).
21. S. Timoshenko and J. N. Goodier, *Theory of Elasticity*, 2nd ed., McGraw-Hill, New York (1951).
22. H. C. Shin and S. I. Pyun, *Electrochim. Acta*, **44**, 2235 (1999).
23. R. Yazami and Y. Reynier, *J. Power Sources*, **153**, 312 (2006).
24. Q. Zhang and R. E. White, *J. Electrochem. Soc.*, **154**, A587 (2007).
25. COMSOL Multiphysics simulation package, available at http://www.it.comsol.com.
26. J. Crank, *Free and Moving Boundary Problems*, Oxford University Press, New York (1984).
27. K. Kumaresan, G. Sikha, and R. E. White, *J. Electrochem. Soc.*, **155**, A164 (2008).
28. J. N. Reimers and J. R. Dahn, *J. Electrochem. Soc.*, **139**, 2091 (1992).
29. Y. M. Chiang, H. Wang, and Y. I. Jang, *Chem. Mater.*, **13**, 53 (2001).
30. D. J. Dunstan, *J. Mater. Sci.: Mater. Electron.*, **8**, 337 (1997).
31. R. H. Perry and D. W. Green, *Perry's Chemical Engineers' Handbook*, 7th ed., McGraw-Hill, New York (1998).
32. D. Aurbach, B. Markovsky, I. Weissman, E. Levi, and Y. E. Eli, *Electrochim. Acta*, **45**, 67 (1999).
33. L. Y. Beaulieu, K. W. Eberman, R. L. Turner, L. J. Krause, and J. R. Dahn, *Electrochem. Solid-State Lett.*, **4**, A137 (2001).
34. D. Wang, X. Wu, Z. Wang, and L. Chen, *J. Power Sources*, **140**, 125 (2005).
35. Y. Itou and Y. Ukyo, *J. Power Sources*, **146**, 39 (2005).